Investigation of the sulphate-induced freezing inhibition effect from CloudSat and CALIPSO measurements

Patrick Grenier[1] and Jean-Pierre Blanchet[1]

Received 19 January 2010; revised 12 July 2010; accepted 23 July 2010; published 18 November 2010.

[1] The hypothesis according to which higher sulphate concentrations favor ice clouds made of larger ice crystals is tested using data sets from the CloudSat and Cloud-Aerosol Lidar and Infrared Pathfinder Satellite Observation (CALIPSO) satellites. This is a potential consequence of the sulphate-induced freezing inhibition (SIFI) effect, namely, the hypothesis that sulphates contribute to inhibit the onset of ice crystal formation by deactivating ice-forming nuclei during Arctic winter. A simple index based on the backscattering at 532 nm and the color ratio from the CALIPSO lidar measurements is compared against in situ sulphate concentration time series and used as a proxy for this variable. An algorithm using the lidar data and the CloudSat radar microphysical retrievals is also developed for identifying cloud types, focusing on those supposedly favored by the SIFI effect. The analysis includes the effect of the lidar off-nadir angle on the sulphate index and the cloud classification, the validation of the index, as well as the production of circum-Arctic maps of the sulphate index and of the SIFI-favored clouds fraction. The increase of the lidar off-nadir angle is shown to cause an increase in the measured depolarization ratio and hence in the ability to detect ice crystals. The index correlates positively with both sulphates and sea salt concentrations, with a Pearson correlation coefficient ($\sqrt{R^2}$) varying from 0.10 to 0.42 for the different comparisons performed. Ultimate findings are the results of two correlation tests of the SIFI effect, which allow for a new outlook on its possible role in the Arctic troposphere during winter.

Citation: Grenier, P., and J.-P. Blanchet (2010), Investigation of the sulphate-induced freezing inhibition effect from CloudSat and CALIPSO measurements, *J. Geophys. Res.*, *115*, D22205, doi:10.1029/2010JD013905.

1. Introduction

[2] Haze in the Arctic occurs frequently and since a long time, with summer events reported by early explorers like Fridtjof Nansen in 1882 and Adolf Erik Nordenskiöld in 1883 [*Garrett and Verzella*, 2008]. The nature and origins of these events are however confidently known only since the 1970s. Arctic haze, mainly a winter and early spring phenomenon, varies in composition, and consists of a mixture of sulphates (compounds comprising the SO_4^{2-} ion) and particulate organic matter, accompanied by smaller mass amounts of ammonium, nitrate, black carbon, dust and other trace constituents [*Law and Stohl*, 2007]. Black carbon may also be a dominant species during certain events [*Hara et al.*, 2003], and the degree of its internal mixing with sulphates increases as the haze ages, as for other compounds. Arctic haze is generally considered to be pollution, since it originates mainly from lower-latitude human activities. Other sources may be volcanoes (releasing sulphate precursor SO_2) and oceanic biota (producing sulphate precursor DMS). Owing to geographic considerations and the winter atmospheric circulation, as well as to their high level of industrialization, Europe and Russia represent the major contributors to the Arctic haze, as inferred from numerical simulations of air pollution transport [*Christensen*, 1997], chemical analysis of trace constituents [*Rahn*, 1981] and vertical extension of haze events [*Carlson*, 1981]. Outside of the concentrated haze patches swept throughout the lower troposphere, a background anthropogenic aerosol exists which extends relatively high into the troposphere. It results from incomplete scavenging by the water content as cyclonic systems pump up aerosols and moisture from lower levels. Unevenly distributed pollution and natural aerosols (e.g., sea salt and mineral dust) constitute the substrate for water condensation and ice nucleation. Hence, they partially determine microphysical properties of the cloud field, in a manner far from being fully understood.

[3] The role of sulphates for the Arctic microphysics may be considered crucial, for at least three reasons. First, sulphates represent the major Arctic aerosol species in terms of mass and relative abundance. For example, of the 18 aerosol constituents studied by *Sirois and Barrie* [1999] between 1980 and 1995, SO_4^{2-} ions alone represent about 50–55% of the mass in January. Also, sulphuric acid covers about 80% of the insoluble particles, as observed by *Bigg* [1980] at

[1]Institut des Sciences de l'Environnement, Université du Québec à Montréal, Montreal, Quebec, Canada.

0148-0227/10/2010JD013905

Barrow, Alaska, and this percentage could be a lower limit [*Blanchet and List*, 1983]. During the ASTAR 2000 campaign over the Svalbard area, *Hara et al.* [2003] also observed that sulphates were the dominant aerosol in terms of relative abundance in particles, under haze as well as background conditions. Our knowledge of the pan-Arctic instantaneous sulphate field (concentrations, proportion of total aerosol mass, internal/external mixing, etc.) is limited. The most reliable information is obtained by local in situ measurements, either during short-duration field campaigns (e.g., ASTAR, AGASP) or at a few permanent stations (e.g., Zeppelin, Alert, Barrow). An alternative way to obtain information about the sulphate field is to numerically simulate transport of sulphur from its emission to its removal points [*Christensen*, 1997]. However, many assumptions must then be introduced. Thus far, no retrieval technique has permitted to isolate sulphate particles from other aerosols and to give their concentration from satellite measurements.

[4] Second, the hydrophilic character of the major sulphate compounds renders them especially effective as cloud condensation nucleus/nuclei (CCN). Indeed, H_2SO_4 particles (sulphuric acid) are hygroscopic, i.e. they grow by absorbing water vapor at any relative humidity with respect to water (RH_w) [*Andreae et al.*, 2008], so that H_2SO_4 does not exist in the crystalline form in the atmosphere. Dry $(NH_4)_2SO_4$ particles (ammonium sulphate) absorb water at RH_w above 80% (deliquescence point) and may return to a crystalline form only below 37% RH_w once wet (efflorescence point), exhibiting a hysteresis behavior. Na_2SO_4 particles (sodium sulphate, the main sea salt sulphate species) have their deliquescence and efflorescence points at 84% and 58%, respectively [*Tang and Munkelwitz*, 1994]. These values are particle size and temperature dependent [*Onasch et al.*, 1999]. Sulphate particles are thus often found within solution droplets in the atmosphere (when not frozen), on one hand causing much light scattering, and on the other hand contributing strongly to cloud initiation. In some numerical model parameterizations, the CCN concentration is determined solely by the sulphate mass concentration [*Lohmann and Roeckner*, 1996; *Lowenthal et al.*, 2004]. This property could have important consequences for the Arctic troposphere ice clouds. Indeed, more sulphates may imply more activated droplets and therefore potentially more ice crystals formed.

[5] The third reason for emphasizing the particular role of sulphates in cloud formation comes from their potential for inhibiting ice nucleation. This effect, which we term sulphate-induced freezing inhibition (SIFI), could explain observations of reduced ice-forming nucleus/nuclei (IFN) concentrations during certain Arctic haze events [*Borys*, 1989], and may have profound consequences on the Arctic cloud cover. At the microphysical level, it is becoming clear that at least one heterogeneous nucleation mode is involved. Laboratory experiments on the deposition mode performed by *Eastwood et al.* [2009] show that kaolinite particles coated with H_2SO_4 require about 30% more ice supersaturation for initiating ice nucleation in the 233–246°K temperature range, whereas $(NH_4)_2SO_4$-coated particles undergo a similar effect at 240°K and 245°K (but a much reduced effect at 236°K). When the supersaturation production rate is high enough for RH_w to reach 100%, liquid droplets may be activated, and subsequent ice nucleation may follow either by immersion/freezing (an IFN acts after having been immersed), by condensation/freezing (the CCN later acts as an IFN during the condensation stage), or by contact (an external IFN touches the droplet surface). We are aware of no laboratory experiment assessing the role of coating in these modes, but we consider that it could be important for contact nucleation, since the involved IFN may cross the droplet surface or rebound without touching it directly, as well as for condensation/freezing at the beginning of the condensation process. It is on the other side probably less important for immersion nucleation and for condensation/freezing once the droplet has become large, since sulphates then get strongly diluted. As for homogeneous freezing, haze droplets require colder temperatures when sulphate concentrations are higher [*Bertram et al.*, 1996]. Laboratory research involving all nucleation modes and a great variety of IFN types is needed for a better understanding of the role of sulphates in ice cloud formation. Given the present state of knowledge, however, it is reasonable to hypothesize that the SIFI is effective within the Arctic troposphere during winter.

[6] The impact of the SIFI on Arctic climate cannot be fully assessed solely from modeling work based on the few laboratory measurements obtained thus far, because the real Arctic IFN mixture shows a large diversity in composition, size, shape and thermodynamic state. Inferences from in situ observations are also limited, owing to the paucity and local character of the measurements. Moreover, the SIFI effect can also not be tested directly from the satellite measurements alone, because we can hardly design a credible proxy for in-cloud sulphate concentrations. Hence, in this paper, we test the SIFI potential consequence according to which higher sulphate concentrations favor cloud populations made of larger ice crystals, caused by a reduction in the competition for water vapor when fewer IFN may operate [*Girard and Stefanof*, 2007]. To achieve this task we have developed the Arctic Winter Aerosol and Cloud Classification from CloudSat and CALIPSO (AWAC4) algorithm. First, it identifies two types of ice clouds (TIC), which are relevant to the present study, one (termed TIC-2B) supposedly favored by high sulphate concentrations at the expense of the other (TIC-2A). As explained in detail in section 3, the crucial difference between these cloud types stems from TIC-2A being topped by a cover of very small (radar-unseen) ice crystals (termed TIC-1), whereas TIC-2B are not. Next, the AWAC4 algorithm assesses the sulphate concentration in non-cloudy probed volumes (bins), via a proxy based on the lidar backscattering fields and validated using ground measurements from the Zeppelin station (in Svalbard Islands, Norway). Finally, the clouds and the sulphate concentration proxy may be spatially characterized, and different correlations relevant to the SIFI effect are calculated and interpreted. This work furthers the previous efforts in this direction made by *Grenier et al.* [2009] (hereinafter GBM).

2. Observational Data Sets

2.1. Satellite Data Sets

[7] The Cloud-Aerosol Lidar and Infrared Pathfinder Satellite Observation (CALIPSO) and CloudSat satellites were launched on 28 April 2006 and joined the A-Train

constellation on a heliosynchronous orbit at an altitude of 705 km. Data sets derived from measurements of their instruments have been described many times in the literature, therefore we merely summarize the information here. Satellites cross the Arctic region 14–15 times per day, with a nadir latitude up to ~82°N.

[8] CALIPSO carries the Cloud-Aerosol Lidar with Orthogonal Polarization (CALIOP) instrument, whose beam hits the ground with a footprint of ~70 m. For this study, we use the total (β_{532}) and perpendicular (β_{per}) attenuated backscattering fields at 532 nm, as well as the total attenuated backscattering field at 1064 nm (β_{1064}). We focus on the lower troposphere, for which the second version (V2) fields are available with 30 m vertical and 333 m horizontal resolutions. *Hunt et al.* [2009] provide further technical details about the mission as well as a performance assessment. Figure 1a shows an Arctic example scene as probed by the lidar (β_{532}) on 5 January 2009. The 3878 juxtaposed profiles (after averaging for mapping on the CloudSat grid) extend from Greenland to the Chukotski Peninsula (trajectory shown in Figure 2).

[9] CloudSat is lagging CALIPSO by about 15 s. Measurements from both platforms are thus nearly coincident in space and time. CloudSat carries the Cloud-Profiling Radar (CPR), with a frequency of 94 GHz (3 mm wavelength). A profile sampling is performed at every ~1100 m on the ground, with a 1.4 × 2.5 km footprint (cross-track × along-track), whereas the vertical sampling is 240 m. *Stephens et al.* [2002] provide an overview of the CloudSat mission. Microphysical properties retrieved from the radar reflectivity (level 1B product) include ice water content (IWC) and ice effective radius (r_{ie}) from the R04 2B-CWC (level 2) product. We used this product for our cloud classification algorithm, and we refer to *Austin et al.* [2009] for details about the retrieval. Since *Kahn et al.* [2007] have found that the radar sensitivity is greatly reduced in the first 3–4 levels just above the surface, we exclude data in the first kilometer above the surface (generally 4 levels, sometimes 5) from the cloud field analysis. This surface contamination effect in the boundary layer data results from the radar pulse length of 1000 m [*Schutgens and Donovan*, 2004]. The R04 ECMWF-AUX temperature field, which consists of the ECMWF analysis interpolated at the CloudSat sampling positions, is also used.

2.2. In Situ Sulphate Concentration Measurements

[10] For this study, we use the winter 2007 (December 2006, January and February 2007) and winter 2008 (hereinafter winter-07 and winter-08) sulphate and sodium concentrations measured at the Zeppelin Mountain Station [*Aas et al.*, 2008]. These are provided by the European Monitoring and Evaluation Programme (EMEP) Chemical Coordinating Centre at the Norwegian Institute for Air Research (NILU; station code NO0042R). Sulphate concentrations have been measured at this station since 1990, with a 24 h time resolution. Geographical coordinates are lat_{Zep} = 78.90°N and lon_{Zep} = 11.88°E. The station is located at 474 m above sea level (asl), which is very often above the temperature inversion. Therefore contamination from local sources is minimal, and average concentrations may be considered representative of what could be measured elsewhere in the region. Air inorganic components are sampled using a 3-stage filter pack, where the front filter (Teflon Gelman Zefluor, with 2 μm pore size) collects particles with an undefined size cutoff. The water extract from the aerosol filter was analyzed using an ion chromatograph. For further technical details, see the EMEP manual [*Norwegian Institute for Air Research*, 1996]. Total sulphate concentrations ($[SO_4 - S]_{tot}$) are provided in units of micrograms of sulphur (S) per cubic meter (μg S / m^3) and are multiplied by the sulphate-to-sulphur mass ratio (3.00) for this study, so that unless otherwise stated the discussed quantity is $[SO_4]_{tot}$. To assess the sea salt contribution in sulphates, we use sodium concentrations ($[Na]$), in μg Na/m^3. Detection lower limit is 0.01 $\mu g/m^3$ for both $[SO_4 - S]_{tot}$ and $[Na]$. For certain days, input concentrations are either invalid (as judged by the data provider) or below the detection limit. In the latter case, we use two thirds of the detection limit. Data from March–April 2000, coinciding with the ASTAR 2000 campaign, are also used for assessing the Arctic haze threshold with the sulphate concentration proxy, as explained later.

2.3. Investigation Period and Domain

[11] Although sulphate concentrations and acidity in the Arctic culminate in April [*Sirois and Barrie*, 1999], the SIFI effect could potentially be most important during winter, when temperatures are coldest. Indeed, supporting field observations by *Borys* [1989] have been performed at −25°C, and supporting laboratory measurements on ice nucleation were conducted at even colder temperatures. Furthermore, the AWAC4 algorithm performance for identifying small crystal size mode ice clouds (TIC-1) is poor in presence of daylight, because of the important solar contamination in the lidar wavelengths. For these reasons, we chose to exclusively investigate the December–January–February nighttime orbital segments of the three winters (2007, 2008, 2009) since the launch of the CALIPSO and CloudSat satellites. For the nine winter months from December 2006 to February 2009, we gathered data from 3143 overpasses, comprising 10 990 147 CloudSat profiles (and ~3.26 times more CALIPSO profiles).

[12] The investigated domain extends from 66.5°N to ~82°N, the northern limit of the A-Train orbit. The farther north an area, the better its satellite coverage, as shown in Figure 2, in which delimitation of the different sectors discussed in this study are also presented. The TIC-2B cloud fraction as well as the sulphate concentration proxy, two variables defined in the section 3, are presented and discussed for the full circum-Arctic investigated zone. However, the different correlations between these fields are computed and/or discussed only for the Eastern Russia–Beaufort Sea–Canadian Archipelago (EBC) sectors, owing to the identification of these sectors by GBM as the most likely to be affected by the SIFI effect.

3. Methodology

3.1. Cloud Identification From Satellite Data

[13] Because the AWAC4 algorithm (v1) has already been detailed by GBM, we only summarize its main steps and present the modifications introduced in the current version (v2). The cloud classification methodology is summarized in Table 1. Input data are submitted to the following treatment: (1) mapping of the CALIPSO fields on the CloudSat grid,

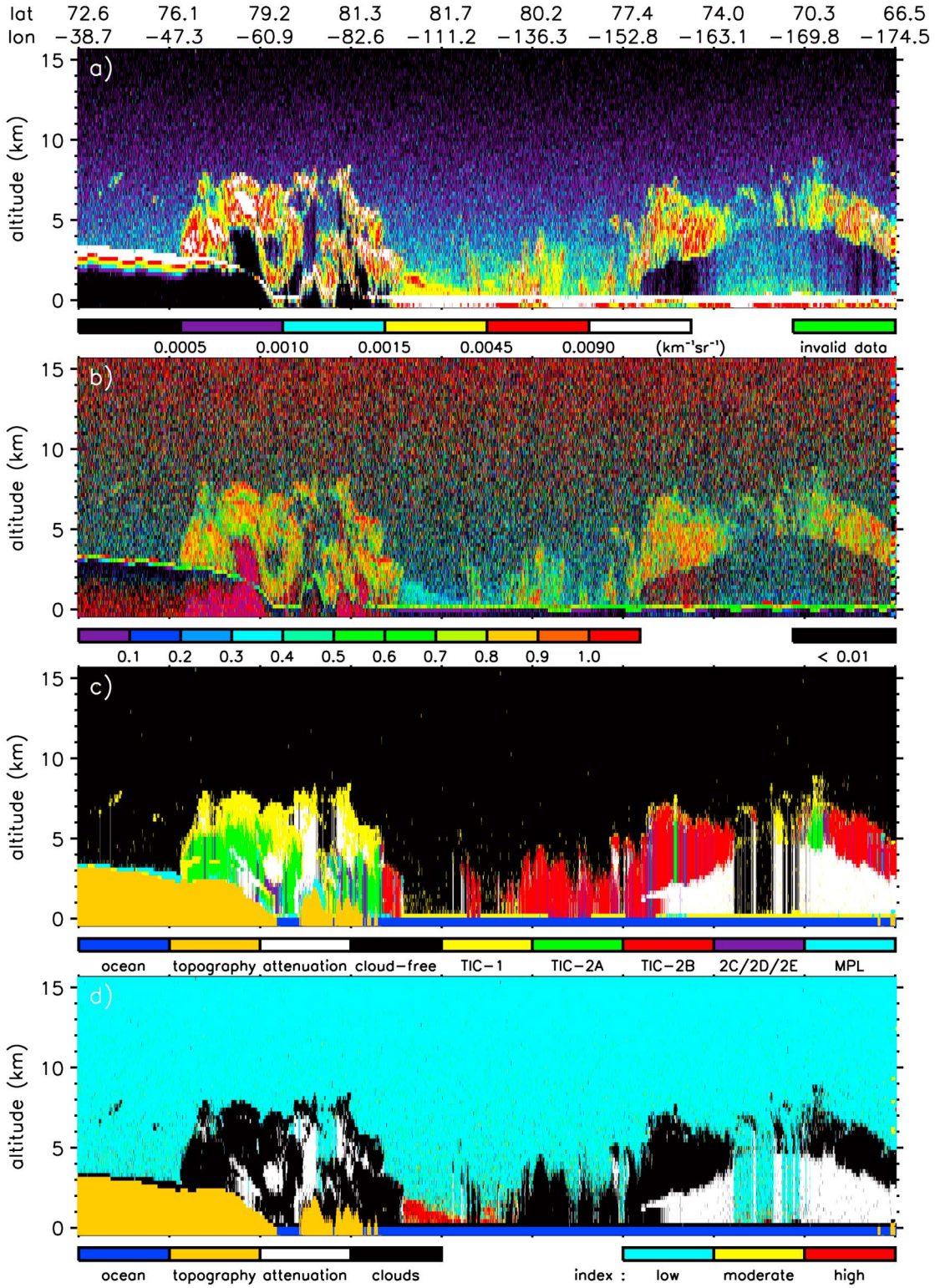

Figure 1. An Arctic example scene, including (a) measured β_{532} (CAL-LID-L1-Prov-V2-02.2009-01-05T14-33-12ZN), (b) color ratio, (c) cloud classification, and (d) aerosol index (weight ratio 2/1). For Figure 1c, CloudSat data in first kilometer above the surface are invalid, so the TIC-2 flags have been filled by extrapolating the above feature for presentation purposes only.

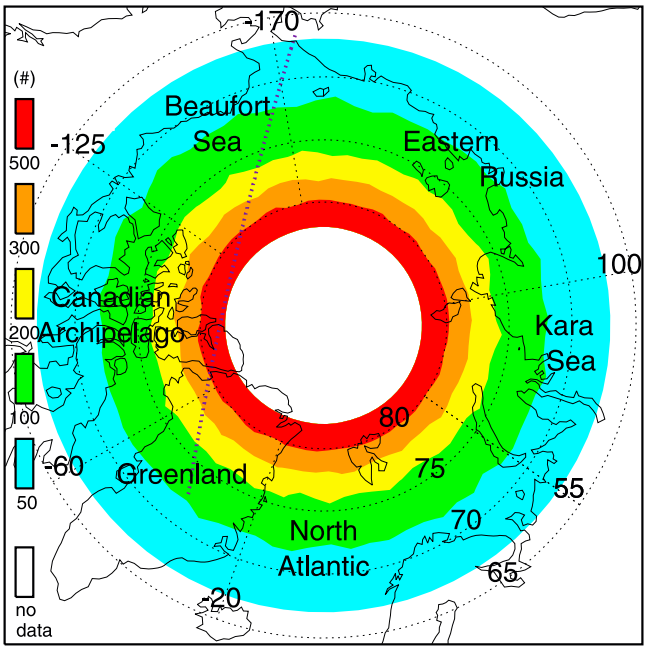

Figure 2. Number of trajectories crossing each 1° × 5° (latitude × longitude) grid box during winter 2008 and winter 2009. Delimitations for inner sectors referred to in the text are also shown, as well as the trajectory of the scene presented in Figure 1 (from Greenland to Chukotski Peninsula).

(2) identification of liquid or mixed-phase layers (MPL) using the sharp β_{532} vertical gradient at their top and base, (3) identification of large ice crystal clouds (TIC-2), for which IWC > 0 in the CloudSat field (not including clouds previously identified as MPL), (4) identification of small ice crystal clouds (TIC-1), for which IWC = 0 but β_{532} and the depolarization ratio ($\delta \equiv \beta_{per} / (\beta_{tot} - \beta_{per})$) values are likely to correspond to ice clouds, and (5) classification of TIC-2 into subtypes (A, B, C, D, and E), depending on the presence or absence of MPL and TIC-1 above. TIC-2C corresponds to ice crystals precipitating below mixed-phase clouds, and these are well identified by the algorithm. The SIFI effect may potentially operate on MPL/TIC-2C systems [*Girard et al.*, 2005], but these are not investigated in this study. The central objective of the AWAC4 algorithm regarding clouds consists of separating as clearly as possible TIC-2A, covered by a TIC-1 layer, from the uncovered TIC-2B, for reasons soon explained. Owing to a great diversity within cloud configurations, this separation is sometimes difficult, so that at the expense of statistics on TIC-2A and TIC-2B systems, we have created two classes of ambiguous cases: TIC-2D, covered by a TIC-1 layer of intermediate thickness, and TIC-2E, for when there is a gap between the TIC-2 and TIC-1 layers. TIC-2B may maximally have 4 TIC-1 bins within the three-profile window above (which comprises the current plus the 2 neighboring profiles). The latter bins may be separated and/or far over the TIC-2B bins, or packed together and right above, in which case they form a layer with an average thickness of 320 m. On average, this layer must extend over at least 800 m (10 bins) to be considered as TIC-2A, in-between cases being identified as TIC-2D (ambiguous thickness case). Juxtaposition of the small and large size mode layers in TIC-1/2A systems is ensured by requiring that at least 70% of the TIC-1 layer (7 bins) lay within the 1200 m (15 bins) just above the TIC-2 layer, otherwise we have TIC-2E (ambiguous gap case).

[14] As for why only some of the TIC-2 are topped by a TIC-1 cover, we consider that the answer first resides in the dependence of ice nucleation on IFN availability and size. When an air mass is cooling, ice particles may start to form when the relative humidity with respect to ice (RH_i) approaches 100%, via the deposition mode. Larger solid aerosol particles, having statistically more active sites, are better IFN, and this size dependence for ice formation efficiency has recently been demonstrated for many dust types in the −20°C to −50°C temperature range [*Welti et al.*, 2009]. Hence, in conditions of stronger vertical motion (higher supersaturation production rate), smaller aerosol particles may also contribute to nucleate ice, increasing the supersaturation sink term and ultimately leading to a cloud made of more numerous and smaller ice crystals (TIC-1). If the vertical movement is sustained, some ice crystals will

Table 1. Summary of the Cloud Classification Method

Cloud Type	Description and Physical Characteristics	Identification Method
Mixed-phase	Clouds with a significant liquid-to-ice ratio, possibly including liquid-only clouds. Flat top. Optically thick. Small vertical extent. Low altitude. Temperature above homogeneous freezing point. High color ratio ($\chi \approx 1$).	Sharp vertical β_{532} gradient at top. $T > -39$°C. Thickness not exceeding 1250 m.
TIC-1	Ice clouds with small size particles, seen by the lidar only. Small ice crystal effective radius ($r_{ie} \leq 30$ μm). Temperature below melting point. High color ratio ($\chi \approx 1$).	Unseen by radar. $T < 0$°C. Not previously identified as mixed-phase or TIC-2. $\beta_{532} \geq \beta_{532\_min} = 0.0009$ km^{-1}sr^{-1}. $\delta \geq \delta_{min} = a_0 + a_1 / \beta_{532}$. Bin surrounded by at least one other TIC-1 bin.
TIC-2	Ice clouds with large size particles, seen by the lidar and the radar. High ice crystal effective radius ($r_{ie} \leq 30$ μm). Temperature below melting point. High color ratio ($\chi \approx 1$).	Seen by radar. $T < 0$°C. Not previously identified as mixed-phase.
2A	TIC-2 under a radar-unseen cloud layer. Covered by a TIC-1 layer.	Important TIC-1 cover ($\Delta h \geq 800$ m).
2B	TIC-2 whose top is seen by the radar. Uncovered by a TIC-1 layer.	No or small TIC-1 cover ($\Delta h \leq 320$ m).
2C	Ice crystals precipitating below a mixed-phase layer.	Immediately below mixed-phase.
2D	Ambiguous thickness case.	TIC-1 cover of intermediary thickness (320 m $\leq \Delta h \leq$ 800 m).
2E	Ambiguous gap case.	Less than 70% of the minimal TIC-1 cover for having TIC-2A lay within 1200 m above the cloud top.

eventually grow to precipitation sizes and aggregate, forming precipitating TIC-2A below the TIC-1 layer. Conversely, in conditions of weaker vertical motion, only large IFN act to form the cloud, leading to a thinner or nonexistent TIC-1 layer above the precipitating TIC-2B layer. This is also consistent with the maximal occurrence of TIC-1/2A systems being found several kilometers above that of TIC-2B, for both highly polluted (e.g., Eastern Russia) and less polluted areas (e.g., Antarctica) (see GBM). When RH_w reaches 100%, the size dependence for ice formation efficiency remains important at least for the immersion mode [*Marcolli et al.*, 2007]. However, *Pruppacher and Klett* [1997] report an absence of studies for size dependence effect of IFN acting in the contact mode and mention that the condensation/freezing mode tends to be less affected than the immersion mode (we have found no recent study concerning these modes in the literature). Despite some arbitrariness in having the criterion used for separating TIC-2A from TIC-2B on the basis of the radar sensitivity, we found after inspection of all the 3143 investigated scenes that the algorithm gives appropriate results, since it is consistent with the previous explanation in three important ways. First, we observe a good profile-to-profile autocorrelation in TIC types, consistent with minimal continuity, which we expect in the synopticomicrophysical conditions giving birth to a cloud system. Second, we often find TIC-1/2A in the center of a cloud cover, with TIC-2B on the sides, but rarely the opposite situation. And finally, TIC-2B are much more likely to present a highly variable top altitude within one structure, suggesting that the majority of ice crystals in their top are precipitating rapidly.

[15] We consider that the SIFI effect superimposes on the size dependence effect and acts to shift the TIC-2 distribution from TIC-2A (with a clear thick TIC-1 top) to TIC-2D (TIC-1 top of intermediary thickness) to TIC-2B (no or thin TIC-1 top). By counting the number (n) of TIC-2B, TIC-2D and TIC-2A bins, we may simply define the TIC-2B fraction among these various cloud cover types (F_{2B}) within specific altitude and time intervals over an area as

$$F_{2B} = \frac{n_{2B}}{n_{2B} + n_{2D} + n_{2A}}. \tag{1}$$

A strong SIFI effect should cause pan-Arctic F_{2B} patterns to present its higher values downwind of the areas showing higher sulphate concentrations (in terms of prevalent circulation during the time interval considered).

[16] For identifying radar-unseen TIC-1 (after the MPL and TIC-2 identification and prior to the TIC-2 subclassification), the algorithm considers first the backscattering at 532 nm, by requiring that $\beta_{532} \geq \beta_{532\_min} = 0.0009\ km^{-1}sr^{-1}$ for a bin to qualify. Next, there is a further requirement that the depolarization ratio (δ) present some minimal value and satisfy

$$\delta \geq \delta_{min} = a_0 + a_1/\beta_{532}, \tag{2}$$

with $a_0 = 10^{-2}$ and $a_1 = 8{\cdot}10^{-5}\ km^{-1}\ sr^{-1}$. The choice for the shape of the δ_{min} function has been discussed by GBM. Parameters have been fixed by trial and error (inspecting the results for many individual scenes similar to that in Figure 1), and by considering the β_{532} and δ distributions. Unfortunately, the haze and TIC-1 distributions overlap in the (β_{532},δ) space. This is partly due to the presence of particles of one feature (aerosol or ice crystals) within probed volumes dominated by the other, and it limits the performance of the algorithm in correctly identifying TIC-1. Finally, TIC-1 bins not surrounded by at least one other of their kind among the eight neighboring bins were declassified, to reduce noise in the TIC-1 signal. The color ratio χ ($\equiv\beta_{1064}/\beta_{532}$) is not used for identifying TIC-1 in the current version of the AWAC4 algorithm.

[17] Figure 1c presents the cloud classification results for the example scene. On the left we may observe TIC-1 bins (yellow) covering TIC-2A bins (green) over Greenland and the Ellesmere Island, with some profiles classified as ambiguous (violet), as well as a TIC-2B (red) area on the western side of the system. On the right half of the scene we see mainly a TIC-2B system, combined with TIC-1/2A and TIC-2D profiles.

3.2. Sulphate Concentration Proxy

[18] We term "cloud free" a bin not labeled as MPL, TIC-2 or TIC-1. Additionally, the bin must not be under any cloud layer, in which case the lidar beam is attenuated and the bin is classified as such. To detect the presence of sulphate particles within these bins, we use an index (α) based on the CALIPSO total attenuated backscattering at 532 nm (β_{532}) and the color ratio (χ) defined as

$$\alpha \equiv \frac{w_\beta \cdot f(\beta_{532}) + w_\chi \cdot g(\chi)}{w_\beta + w_\chi}, \tag{3}$$

$$f(\beta_{532}) = \min\left(\max\left(0, \beta_{532}/\beta_{ref}\right), \beta_{ref}\right), \tag{4}$$

$$g(\chi) = \max(0, 1 - m \mid \chi - \chi_0 \mid). \tag{5}$$

This lidar-derived index is a new version of that used by GBM, in which the constants w_β and w_χ represent weights for the backscattering (first) and color ratio (second) terms. The function $f(\beta_{532})$, corresponding to the β_{532}/β_{ref} ratio bounded between 0 and 1 (the maximum value is set if $\beta_{532} \geq \beta_{ref} = 0.0030\ km^{-1}\ sr^{-1}$), reflects the expectation that the presence of sulphate particles among air molecules contributes to increase the backscattering. A caveat with this term stems from the existence of other aerosol compounds and especially of ice crystals in bins classified as cloud free, which may significantly contribute to raising of the index. By giving weight to $g(\chi)$, a triangular function with amplitude 1 at its center $\chi_0 = 0.35$ and nonzero values only between 0.15 and 0.55 ($m = 5$), we limit the effect of the ice crystals on the index, because $\chi \cong 1$ for clouds [*Wandinger*, 2005; *Liu et al.*, 2002]. This function also ensures that bins with small aerosol loadings score low in the α index, since $\chi_{molecular} \cong 1/16$ in virtue of the λ^{-4} dependence for Rayleigh scatterers [*Wandinger*, 2005]. However, owing to small β_{532} and β_{1064} signal-to-noise ratios in molecular bins, the color ratio field is too noisy in these circumstances for the second term of equation (3) to be given full weight. The parameters of the triangular function have been chosen considering the theoretical work of *Liu et al.* [2002], which have inferred from LITE observations that the frequency of

occurrence of integrated attenuated color ratio for aerosol layers is highest in the interval $0.15 < \chi \leq 0.55$ (approximately; their probability function is not triangular). Figure 1b shows the color ratio field for the example scene. Clouds, identified independently of the color ratio, appear with values ranging from a minimum of about $0.50 < \chi \leq 0.60$ to a maximum above 1.0. For cloud free and relatively clean air (at high altitudes), the signal is very noisy (the noise is reduced after the mapping on the CloudSat grid by setting β_{532} and β_{1064} minimal threshold values at $1{\cdot}10^{-5}\ km^{-1}\ sr^{-1}$ and $\chi_{molecular}{\cdot}10^{-5}\ km^{-1}\ sr^{-1}$, respectively). Between longitudes −82.6°E and −111.2°E, we see a singular feature (pale blue) contrasting strongly with the adjacent cloud cover. These color ratio values ($0.30 < \chi \leq 0.40$) lead to high α values, as shown in Figure 1d.

[19] It is generally considered that frozen water, humidity and sulphates account for nearly all the light scattering from Arctic haze [*Arctic Monitoring and Assessment Programme*, 1998], but other major aerosol types found in the Arctic also contribute to raise $f(\beta_{532})$ above the value for sulphates only. We do, however, expect this contribution to be limited. For instance, soot particles cannot contribute strongly to raise this term of equation (3), even though they scatter light as small individual particles [*Clarke*, 1989]. Indeed, they have a marginal effect on the backscattering when mixed internally within haze [*Blanchet and List*, 1983], where they generally represent about 5% of the total aerosol mass [*Shaw et al.*, 1993] and rather act as absorbers. Likewise, giant sea salt particles are expected to scatter light less efficiently than fine sulphate particles for a same mass concentration [*Waggoner and Weiss*, 1980]. A high sea salt mass concentration, as observed during sodium storm events (sudden and short-duration [*Na*] increase), can cause much scattering. However, because maritime mixtures under high relative humidity are most likely to present attenuated color ratio values around 0.7 [*Liu et al.*, 2002], their score in $g(\chi)$ is a priori expected to be low. This is linked to the color ratio being considered a good proxy of the size of the probed particles [*Omar and Babakaeva*, 2004], with smaller color ratios associated with smaller aerosol particles. However, scattering from very large particles (comparatively to 1064 nm in our case) does not respect that dependence on wavelength, and clouds generally exhibit $\chi \cong 1$. Owing to their large size, dust and marine aerosols can also exhibit χ values near or even above 1, whereas for aerosol mixtures containing much pollution (including submicron-size sulphate particles) the color ratio should be much smaller than 1 [*Omar and Babakaeva*, 2004]. It must, however, be kept in mind that the aerosol fine (submicron) mode is not exclusively composed of sulphates. Using Terra MODIS collection 5 (collection 4) data over various oceanic regions, *Yu et al.* [2009] have retrieved fine mode fractions of 0.90 (0.92) for pollution, 0.37 (0.51) for mineral dust and 0.45 (0.32) for the natural marine aerosol. These numbers vary spatially and seasonally, but the values suggest that other aerosol compounds contribute to raise $g(\chi)$ less than Arctic haze compounds do.

[20] From the previous considerations, we expect α to be a reasonable sulphate concentration proxy, with higher values potentially indicative of Arctic haze events. This proxy must, however, be validated. Unfortunately, only a few sulphate concentration time series are available for the Arctic, station locations are seldom comprised within the instruments footprint when satellites fly over the area, and cloud cover often hinders the calculation of α. We are then obligated to average α over a wide zone. Furthermore, when the station is located at an altitude too low, the sulphate concentration must be compared with the proxy calculated and averaged for a higher altitude layer. At the moment of doing the analysis, in situ sulphate concentration data sets from three monitoring Arctic sites were available: Zeppelin (78.90°N, 11.88°E, 474 m asl, daily averaged), Alert (82.47°N, 62.50°W, 100 m asl, weekly averaged) and Barrow (71.30°N, 156.60°W, 8 m asl, daily averaged). Each station presents advantages and drawbacks in regards to the validation/calibration of α. After analysis of the satellite overpasses around each site, it appeared to us that only data from Zeppelin could be used for the present study. The Barrow station has data usable only for precise wind conditions due to possible local contamination; its satellite coverage is small and its altitude too low. Problems with the Alert station come from a location latitude too high for the satellite overpasses, combined with the high elevation of Greenland and Ellesmere Island on its southern side, which prevents from averaging α around the site and at a comparable altitude. These geographical limitations are not encountered at the Zeppelin station. However, because it is located in the North Atlantic sector, the frequent cloud cover reduces the statistics and the marine aerosol has more influence on the calibration of α. Details of the comparison procedure are discussed in section 4.2.

[21] A major difference in the way CALIPSO data were collected during the investigation period stems from the fact that the CALIOP instrument has been reoriented at an off-nadir angle (ONA) of 3.0° at the end of November 2007 (this angle was previously 0.3°). It is well known that the depolarization ratio, used for identifying ice crystals (TIC-1), is sensitive to the off-nadir angle [*Sassen*, 1991]. Indeed, in presence of plate-like horizontally oriented crystals, increasing ONA results in higher depolarization values (M. Vaughan, Lidar pointing angle change, NASA Langley Research Center, Langley, Virginia, 2008; available at http://eosweb.larc.nasa.gov/PRODOCS/calipso/pdf/TiltModeGeometry.pdf). This causes further biases in cloud and sulphate detection, as discussed later.

3.3. In Situ Data

[22] Because coarse aerosol particles like sea salt are less likely to exhibit small color ratio values than particles in the accumulation mode are, we correct sulphate concentrations observed at the station by removing the contribution of sea salt from the total measured value. Considering a mass concentration ratio $[SO_4]$ / $[Na]$ = 0.252 in the seawater composition [*Broeckner and Peng*, 1982], the following formula is used for assessing the non-sea-salt (nss) sulphate mass concentration:

$$[SO_4]_{nss} = [SO_4]_{tot} - 0.252[Na]. \quad (6)$$

This correction may be important, as we found that average sea salt contribution in the sulphate concentrations measured at Zeppelin was 20% during both winter-07 and winter-08. Sea salt has the potential to increase the mean diameter of sulphate aerosols by up to a factor of 2 over the marine

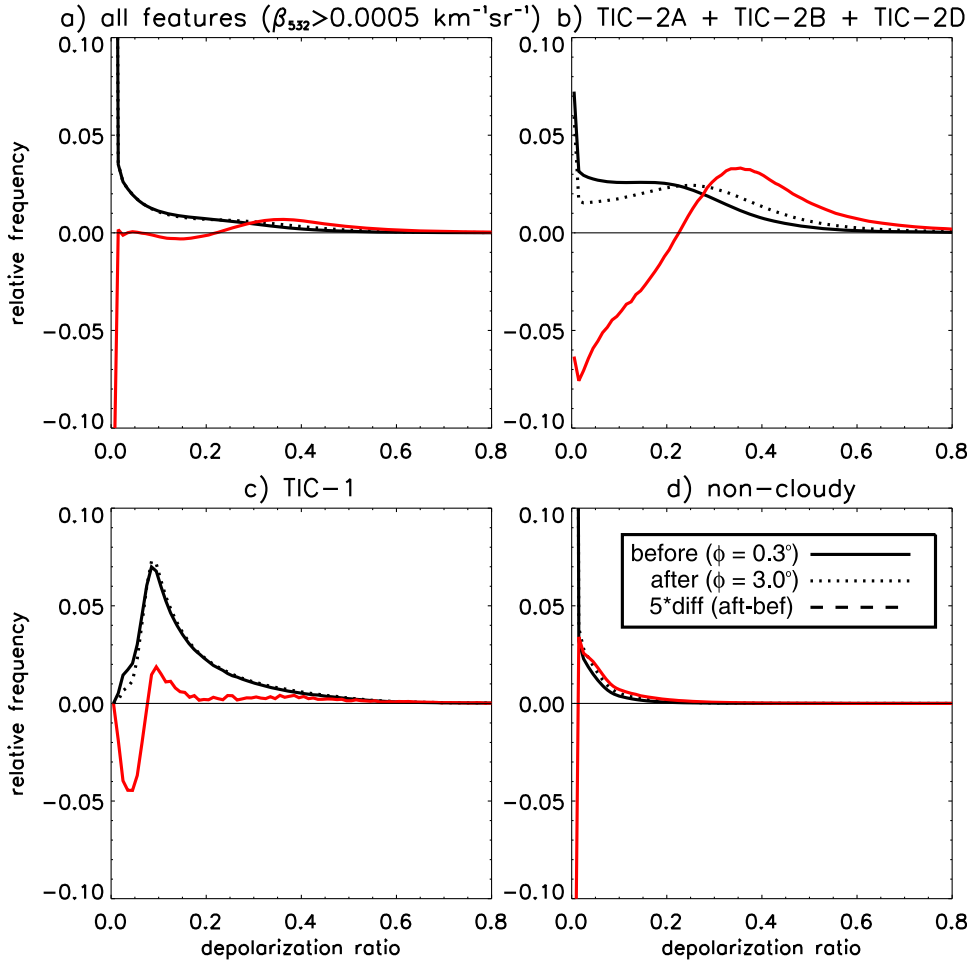

Figure 3. Normalized δ distributions for (a) all bins, (b) TIC-2A + TIC-2B + TIC-2D, (c) TIC-1, and (d) haze. Thickness of the bins is $\Delta\delta = 0.01$. Differences are magnified by a factor of 5 for better visual appreciation.

boundary layer [*Gong and Barrie*, 2003]. The color ratio signal may thus be affected, with a considerable fraction of the sulphate mass not detected. A priori, we did expect α to correlate better with $[SO_4]_{nss}$ than with $[SO_4]_{tot}$.

4. Main Results

4.1. Lidar Off-Nadir Angle Effect

[23] The algorithm applied to input data is the same for all investigated scenes, but a bias may result from the increase in the lidar off-nadir angle (ONA) performed between winter-07 and winter-08. An expected change from the modification of this instrumental variable is an increase of the depolarization ratio (δ) from ice crystals, since specular reflection on horizontally oriented plates is reduced by an ONA increase [*Sassen*, 1991].

[24] Visualization of the 3143 scenes (cloud classification and the sulphate concentration proxy α) clearly shows that ONA increase has an impact on the TIC-1/aerosol separation in the upper troposphere. At these altitudes, the probability of finding a highly concentrated aerosol layer is low, and we can identify with a high level of confidence the high α features which should be classified as TIC-1, mainly by verifying the continuity in their spatial structure. Between 5 km and 12 km altitudes, we estimate that the AWAC4 algorithm misclassifies vast portions of TIC-1 in about 22%, 13% and 20% of the scenes during December 2006, January 2007, and February 2007, respectively. This percentage falls below 1% for all months after ONA increase (with a comparable proportion of scenes containing TIC-1 at these altitudes for all months). Most affected TIC-1 have no TIC-2A extension and generally consist of horizontally wide features (extending over hundreds of kilometers).

[25] Lower in the troposphere, it is harder to quantify the impact of ONA increase, since aerosol layers are likely to be found juxtaposed to or in-between cloud systems. We could therefore find no clear evidence of a TIC-1 distribution change simply by visualizing the scenes. Figure 3a shows the normalized δ distributions for all bins satisfying $\beta_{532} \geq 0.0005$ km^{-1} sr^{-1} and within the altitude range 1000–5000 m. Curves show that after ONA increase, there were fewer bins with $\delta \sim 0$, but more in the range $\delta \sim 0.2$–0.6, as expected. However, a change in the relative abundance of haze and clouds could potentially mimic the ONA change effect. It is not clear which effect dominates, but both could be important. The shift to the right in the radar-seen (TIC-2A + TIC-2B + TIC-2D) δ distribution (Figure 3b) can only be explained by the ONA change (unless we

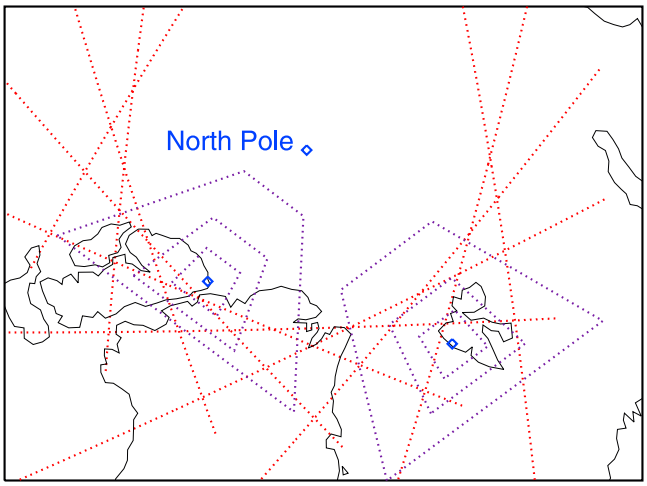

Figure 4. Nighttime coverage around Zeppelin (left diamond) and Alert (right diamond) stations, for a 24 h period (27 January 2007). Box sizes are 250, 500, and 1000 km (side).

suppose that a change in the average vertical movement has caused a change in the proportion of horizontally oriented ice crystals, but results are similar if we consider only TIC-2B, which are expected to be associated with slower vertical movement). The peaks near $\delta \sim 0$ in Figure 3b are most likely due to molecular or haze contribution just above TIC-2 tops. The δ distributions for aerosols (Figure 3d) and TIC-1 (Figure 3c) are also consistent with expected consequences from ONA increase. Indeed, in the first case we expect a shift to the right caused by the small amount of crystals present within these bins, whereas in the second case we expect the shift to be different from that for TIC-2, since bins which would have been classified as haze (had the lidar not been inclined) enter the TIC-1 δ distribution from the left side.

[26] Therefore, it is reasonable to conclude that the lidar inclination has a real influence on the haze/TIC-1 partake, and consequently on the average sulphate index and the TIC-2A/TIC-2B partake (since TIC-2A are defined by the existence of an overlaying TIC-1 layer). For this reason, it is important to analyze both periods (before and after ONA increase) separately. Changes in the abundance ratios estimated with our algorithm could also partly come from changes in the "true" abundances between winter-07 and the two subsequent winters, since the χ distributions for all bins (satisfying $\beta_{532} \geq 0.0005\ km^{-1}\ sr^{-1}$) also change (not shown), whereas we found no mention in the literature on how the lidar ONA could affect this variable (this issue remains unanswered by the scientific community).

4.2. Validation of the Proxy

[27] We have compared daily averaged concentrations of sodium and sulphate (as well as their sum and nss-sulphate) from Zeppelin in situ data to the index α, within a geographical box centered on Zeppelin. For the index, three box sizes have been tested (250, 500 and 1000 km), as shown in Figure 4 (also shown for Alert, Canada). It appeared that for both winter-07 and winter-08, index series for 500 km better reproduce the in situ data than the index series for 1000 km do. For their part, index series for 250 km offer too few observation data to provide a reliable comparison. The validation exercise therefore focuses on the 500 km series. This represents a compromise between minimizing the footprint-to-station distance and having enough points to average for most days. For instance, borders for the 500 km box are determined by setting $lat_{\min}$ and $lat_{\max}$ at 250 km southward and northward of lat_{Zep}, and by setting $lon_{\min}$ and $lon_{\max}$ at 250 km westward and eastward of lon_{Zep} at the lat_{Zep} latitude. The index is averaged for each day by considering all values within the altitude interval from 224 m above ground level to 724 m asl. Certain of the daily point pairs have been ignored in the subsequent analysis, because either in situ data were flagged invalid by the data provider or there were less than $n_{\min} = 100$ satellite index values to average.

[28] Figure 5 shows three curves for each winter: $[SO_4]_{tot}$, $[Na]$ and $\alpha_{2/1}$ (with a 2/1 weight ratio in equation (3)). Comparison of the curves suggests that the index is sensitive to both the Arctic haze and the marine aerosol, since most $\alpha_{2/1}$ peaks correspond to either a $[SO_4]_{tot}$ or a $[Na]$ maximum. In particular, it seems clear that sea salt is involved in the $\alpha_{2/1}$ peaks of day 27 and day 58 during winter-07, whereas Arctic haze caused the marked increase in the index for days 44–49 of winter-07. Moreover, there are periods of low $[SO_4]_{tot}$ and $[Na]$ during which the index remains relatively low (first days of winter-07 and days 40–60 of winter-08). Conversely, peaks often mismatch by one or two days, and an important $[SO_4]_{tot}$ peak during the last days of winter-08 is not reflected by a comparatively important $\alpha_{2/1}$ peak. Numerically, we may assess the correspondence between the curves by calculating the Pearson correlation

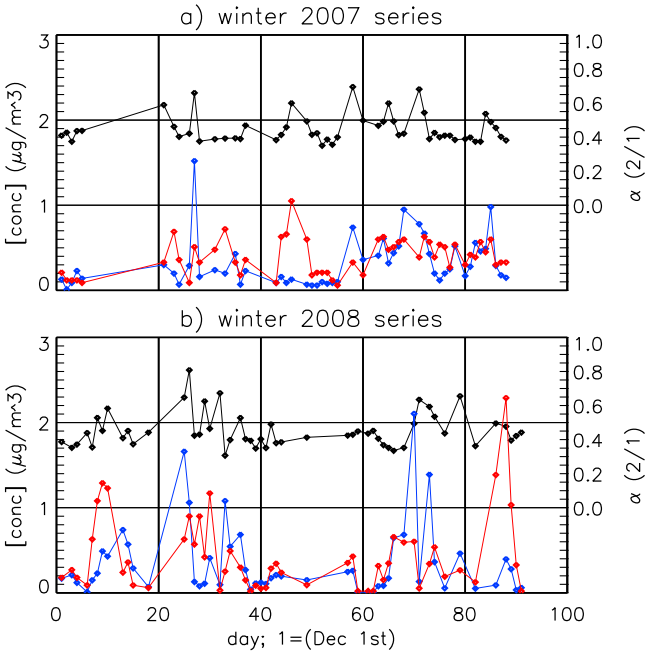

Figure 5. Comparison of the sulphate concentration proxy ($\alpha_{2/1}$, black curve) averaged in the 500 km wide box around Zeppelin station with in situ $[SO_4]_{tot}$ (red curve) and $[Na]$ (blue curve) measurements for (a) winter 2007 and (b) winter 2008.

Table 2. Pearson Correlation Coefficient ($r_{Pea} = \sqrt{R^2}$) Between In Situ Concentrations and Proxy (α) Series, With 95% Confidence Intervals as Obtained Through Fisher's z-Transformation Test[a]

	$f(\beta_{532})$	5/1	2/1	1/1	1/2	1/5	$g(\chi)$
$[SO_4]_{tot}^{all}$	$0.20_{0.01}^{0.38}$	$0.22_{0.03}^{0.39}$	$0.23_{0.04}^{0.41}$	$0.25_{0.06}^{0.42}$	$0.27_{0.08}^{0.44}$	$0.29_{0.10}^{0.46}$	$0.30_{0.12}^{0.47}$
$[SO_4]_{nss}^{all}$	$0.10_{-0.01}^{0.29}$	$0.11_{-0.08}^{0.30}$	$0.13_{-0.06}^{0.31}$	$0.15_{-0.04}^{0.33}$	$0.18_{-0.01}^{0.36}$	$0.20_{0.01}^{0.38}$	$0.23_{0.04}^{0.40}$
$[Na]^{all}$	$0.40_{0.23}^{0.55}$	$0.40_{0.23}^{0.55}$	$0.40_{0.23}^{0.55}$	$0.39_{0.22}^{0.54}$	$0.38_{0.20}^{0.53}$	$0.35_{0.17}^{0.51}$	$0.30_{0.12}^{0.47}$
$[SO_4]_{tot}^{all} + [Na]^{all}$	$0.42_{0.24}^{0.56}$	$0.42_{0.25}^{0.57}$	$0.42_{0.25}^{0.57}$	$0.42_{0.25}^{0.57}$	$0.41_{0.24}^{0.56}$	$0.39_{0.22}^{0.54}$	$0.35_{0.17}^{0.51}$
$[SO_4]_{tot}^{sub}$	$0.17_{-0.03}^{0.37}$	$0.19_{-0.01}^{0.39}$	$0.22_{0.01}^{0.41}$	$0.25_{0.05}^{0.43}$	$0.28_{0.08}^{0.46}$	$0.31_{0.11}^{0.49}$	$0.34_{0.14}^{0.51}$
$[SO_4]_{nss}^{sub}$	$0.17_{-0.04}^{0.36}$	$0.19_{-0.02}^{0.38}$	$0.21_{0.01}^{0.40}$	$0.24_{0.04}^{0.43}$	$0.27_{0.07}^{0.45}$	$0.30_{0.10}^{0.48}$	$0.32_{0.12}^{0.49}$
$[Na]^{sub}$	$0.08_{-0.12}^{0.29}$	$0.10_{-0.10}^{0.30}$	$0.13_{-0.08}^{0.33}$	$0.16_{-0.05}^{0.35}$	$0.19_{-0.01}^{0.38}$	$0.23_{0.03}^{0.42}$	$0.26_{0.06}^{0.45}$
$[SO_4]_{tot}^{sub} + [Na]^{sub}$	$0.15_{-0.06}^{0.34}$	$0.17_{-0.04}^{0.36}$	$0.20_{-0.01}^{0.39}$	$0.23_{0.03}^{0.42}$	$0.27_{0.07}^{0.45}$	$0.32_{0.12}^{0.49}$	$0.35_{0.16}^{0.52}$

[a]The ratio above each column corresponds to the ratio of the weights given to $f(\beta_{532})$ and $g(\chi)$ in equation (3), with full weight given to one term in the $f(\beta_{532})$ and $g(\chi)$ columns. Label "all" means the whole series (105 points) are used, whereas label "sub" means sodium storms have been ignored (91 points left).

coefficient ($r_{pea} = \sqrt{R^2}$). Results are found in Table 2, first for all points shown in Figure 5. It appears that for all weight ratios tested, the sum ($[SO_4]_{tot}^{all} + [Na]^{all}$) correlates best with the index, as compared with the components considered individually and with $[SO_4]_{nss}^{all}$ Series for $[SO_4]_{tot}^{all}$ and $[Na]^{all}$ correlate equally well with $g(\chi)$, but adding weight to $f(\beta_{532})$ improves the correlation for sodium whereas it worsens it for sulphates. Removing the sea salt portion of sulphates leads to lower r_{pea} whatever the weight ratio. As it is clear from Figure 5 that sodium storms strongly modulate the index values, we also performed the r_{pea} calculations for a subset of points, excluding those for which $[Na] > 2 \cdot [Na]^{all} = 0.66\ \mu g/m^3$ (this concerned 14 out of 105 daily values over the two winters). Results (Table 2) show that ignoring sodium storms leads to higher r_{pea} between total sulphate concentrations and the index if $w_\beta < w_\chi$. We ensured that 224 m above the surface was high enough to avoid possible contamination of the results from the surface reflection (which could be introduced via errors in the input topographic files or the mapping procedure of CALIPSO data on the CloudSat grid) by redoing the validation exercise with the altitude interval 474–724 m asl and achieving practically identical results for Figure 5 and Table 2. We also ensured that the mid-January peaks correspondence between $\alpha_{2/1}$ and $[SO_4]_{nss}^{all}$ was not an artifact from misclassified TIC (scoring high in $f(\beta_{532})$) by closely inspecting the color ratio in each of the 14 scenes involved. Certain high $\alpha_{2/1}$ bins are misclassified TIC in one scene of day 44 and one of day 45, whereas the high $\alpha_{2/1}$ features recorded on days 46 and 49 were clearly aerosol layers ($0.30 < \chi \leq 0.40$).

[29] Although results from Table 2 should lead to the use of 0/1 ($\alpha_{0/1}$) as the working weight ratio for later applications of equation (3), we rather adopted 2/1 ($\alpha_{2/1}$). This choice stems primarily from the low signal-to-noise ratio in the color ratio (especially when β_{532} remains low), and second from the design of $g(\chi)$, which for example has the same value whether $\chi = 0.20$ or $\chi = 0.50$, whereas in principle the signal should be more dominated by smaller particles in the first case. The color term has been designed to roughly reveal objects in the range $0.15 < \chi \leq 0.55$, but the choice of a triangular function is admittedly arbitrary. For most subsequent results, we briefly refer to the effect of using $\alpha_{0/1}$ instead of $\alpha_{2/1}$. By visual inspection of the relevant fields (β_{532}, χ, δ, α and TIC-1) for several scenes, 2/1 appears as the best weight ratio for contrasting extended aerosol features against the background signal. Overall, both terms in equation (3) are of importance.

[30] The initial objective of comparing α with measured sulphate concentrations was to perform a calibration for the entire Arctic region. While Svalbard Islands are located in North Atlantic and exposed to sodium storms, this is not the case for most of the Arctic, since giant sea salt particles are not likely to be blown far from the sea ice/open waters edge. In this context, we think the best approach for calibrating the index on sulphate concentrations is to use $[SO_4]_{tot}^{sub}$, which correlates positively with α, and we obtain the following linear regression (bounded at a minimal value of zero):

$$[SO_4]_{tot} = 7.7 \cdot \max\left(0, \alpha_{2/1} - 0.42\right). \quad (7)$$

Although equation (7) is based on a statistically significant correlation between daily averaged values, we use this calibration equation only to estimate the sulphate concentrations. Of course, the results of its application over North Atlantic and Kara Sea must be interpreted carefully, since these sectors are often devoid of sea ice cover during winter, and therefore sea salt is expected to impact the $\alpha_{2/1}$ signal. Additionally, this calibration is unreliable for any single bin. One important reason for considering equation (7) is that it offers a simple method for identifying Arctic haze. As far as we know, there exists in the literature no definition of an Arctic haze event in terms of a minimal sulphate concentration at the ground. These events are rather identified on the basis of optical properties of the aerosol loading aloft. To obtain a reasonable $[SO_4]_{tot}$ threshold for Arctic haze, we use data from the ASTAR 2000 campaign (12 March to 25 April), when *Yamanouchi et al.* [2005] observed a frequency of Arctic haze situations 40% of the time in the Svalbard area. Investigating the Zeppelin station $[SO_4]_{tot}$ for that period, we found that 40% of the daily averaged concentration values were above $[SO_4]_{haze\_min} = 0.96\ \mu g/m^3$, a threshold corresponding by equation (7) to $\alpha_{haze\_min} = 0.54$. Because pollution layers may be vertically highly inhomogeneous [*Quinn et al.*, 2007], the correspondence between an optically identified Arctic haze event and a sulphate concentration above $[SO_4]_{haze\_min}$ at the ground is likely to fail for any single day period. When applied over a longer period, however, we think the threshold may give a reasonable indication of the Arctic haze frequency (for non-cloudy conditions). This threshold has been used in Figure

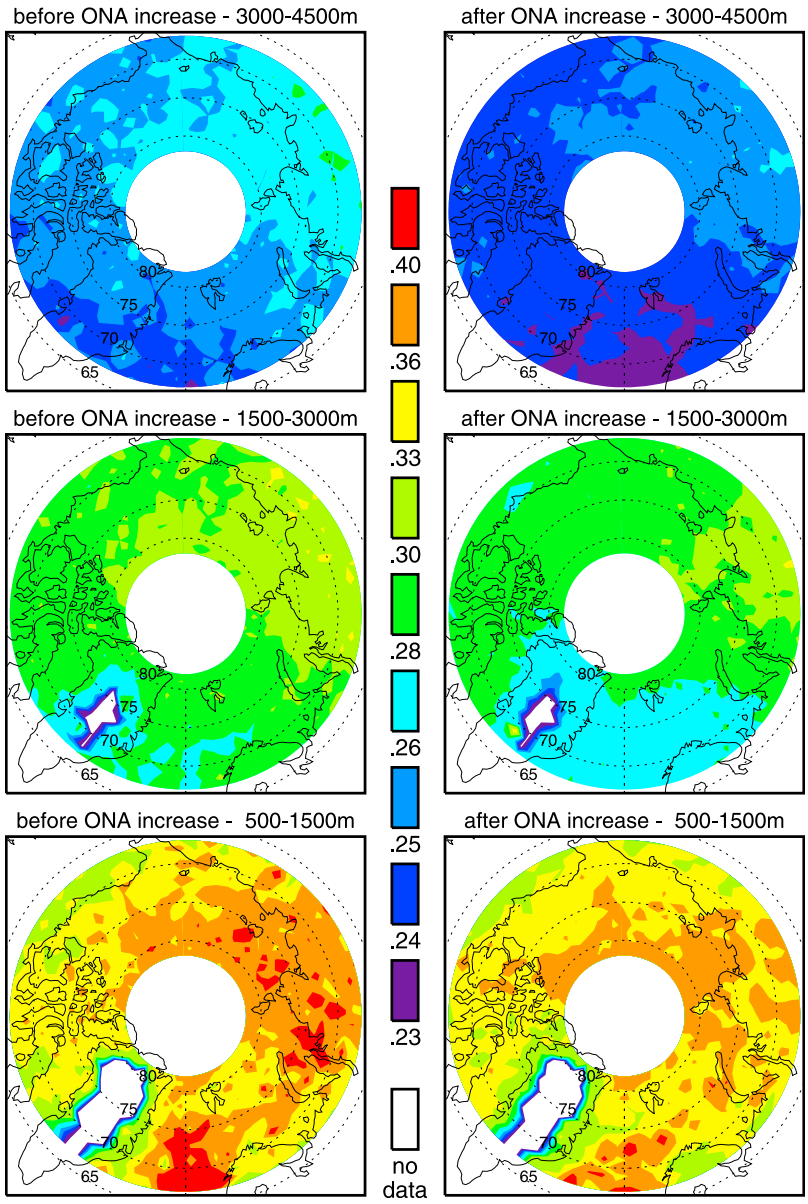

Figure 6. Average index ($\alpha_{2/1}$) (left) before ONA increase and (right) after ONA increase, for different layers.

1d as the minimal value for the "high index" interval. The group of red bins in the middle indicates that the lidar likely encountered an Arctic haze event.

4.3. Circum-Arctic Index Distribution

[31] The index ($\alpha_{2/1}$) derived from the CALIPSO data has been used to create an index map centered on the North Pole. All values compiled during the investigated period within each 1° × 5° (latitude × longitude) grid box have been averaged. Results are presented in Figure 6 for three different altitude layers and for the two periods separated by the ONA increase (a band of 500 m above ground level is ignored). The patterns here are more relevant to consider than exact numerical index values. Probably the most striking characteristic of Figure 6 is the marked difference between the pre- and post-ONA increase index values, due to better TIC-1 classification in the latter case. However, the general pattern is preserved. In both cases we see that the index generally decreases with height. In the lowest layer (500–1500 m), highest values occur over North Atlantic, Eastern Russia and Beaufort Sea (see Figure 2 for delimitations of the sectors we refer to), whereas above 1500 m North Atlantic becomes the sector with the lowest index values. The fact that the high $\alpha_{2/1}$ feature over North Atlantic has no extension above 1500 m renders us confident that it mostly corresponds to coarse sea salt particles, and that relatively high $\alpha_{2/1}$ values above 1500 m correspond to small sulphate and companion particles originating from Eurasian human activities. Using $\alpha_{0/1}$ instead of $\alpha_{2/1}$ produces similar patterns.

4.4. Circum-Arctic TIC-2B Fraction

[32] Using the same data grid as for $\alpha_{2/1}$, we have calculated the average F_{2B} during the investigation period (the

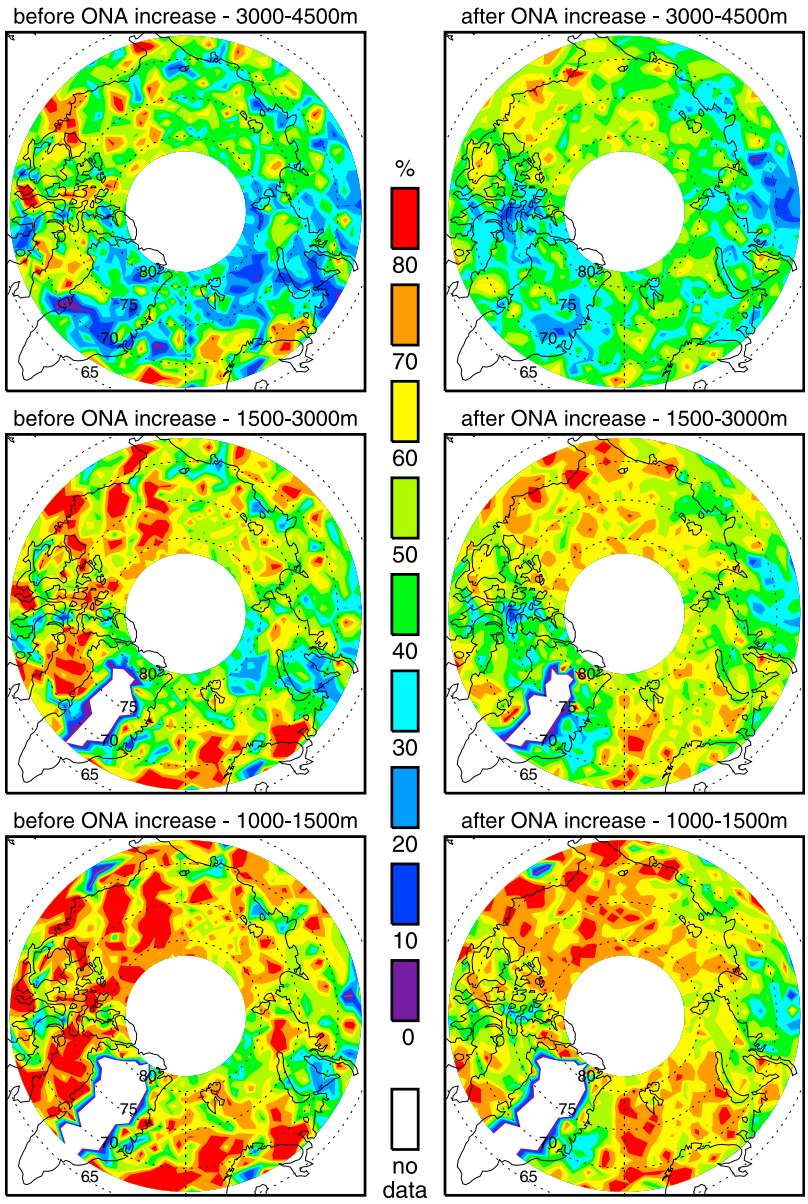

Figure 7. Average TIC-2B fraction (F_{2B}) (left) before ONA increase and (right) after ONA increase, for different layers.

division in equation (1) is performed after the total numbers of TIC-2A, TIC-2D and TIC-2B bins are determined). Results are presented in Figure 7. Again, we see an important difference between the pre- and post-ONA increase, consistent with a better identification of TIC-1 and hence TIC-2A after ONA increase, which raises the denominator in equation (1) and hence lowers F_{2B}. The adopted color scale reveals clearer patterns after ONA increase, when for all layers we have higher F_{2B} values over North Atlantic, Beaufort Sea and the eastern part of Eastern Russia. Before and after ONA increase, Kara Sea, Greenland and the western part of Eastern Russia generally had lower TIC-2A fractions relative to the other sectors. The situation differs for the Canadian Archipelago, since we find high values relative to other locations only before ONA increase. This may be due to a particular circulation pattern during winter-07.

4.5. Ice Effective Radius–Index Correlation

[33] GBM reported calculation results of the linear correlation coefficients between CloudSat retrieved r_{ie} values at the top of TIC-2B (averaged over the 3 upper bins) and the aerosol index just above (averaged within the 6 closest bins, TIC-1 excluded). We had obtained $r_{pea} \in [0.09,0.15]$ for the different Arctic sectors, and interpreted this result as an indication of a real SIFI effect. In the current study, we performed a similar calculation, considering all TIC-2B profiles within EBC sectors after ONA increase. Differences with the previous methodology were (1) the consideration of only the second to the fourth bins above the cloud (rather

than the first to the sixth), (2) a modified index, (3) the domain, (4) the ONA, and (5) the segregation of the series by height intervals. The goal of ignoring the first bin was to avoid possible contribution of TIC-2B ice crystals to $\alpha_{2/1}$ in the bottom of the bin just above, whereas that of segregating calculations by height intervals was to avoid a false signal coming from the height dependence of $\overline{r_{ie}}$ and $\alpha_{2/1}$. Pairs of points ($\overline{r_{ie}}$,$\alpha_{2/1}$) were grouped according to the bin number of the highest TIC-2B bin in a profile, starting at ~1200 m and ending at ~6500 m (asl) with 240 m thick intervals. The number of points entering the correlation calculation varied between ~20 000 and ~30 000 for each bin interval. We did not find systematic positive and significant r_{pea}. Instead, r_{pea} remained confined within ~±0.02, with statistically significant values at the 95% level (through Fisher's z-transformation test) for a few height intervals only. Varying the methodology by considering (1) the first bin above the TIC-2B top, (2) $\alpha_{0/1}$, (3) all Arctic sectors, or (4) only the period before ONA increase did not change the results qualitatively. However, merging all pairs of points in a single series (no matter the height of the TIC-2B top) led to positive and statistically significant results, i.e. $r_{pea} = 0.167^{0.170}_{0.163}$ before ONA increase and $r_{pea} = 0.158^{0.160}_{0.155}$ after (using $\alpha_{2/1}$; comparable results using $\alpha_{0/1}$). In sum, making a deeper analysis of the correlation between r_{ie} at the top of TIC-2B and $\alpha_{2/1}$ just above has provided no proof that sulphates favor cloud populations made of larger ice crystals. Moreover, the signal interpreted by GBM as supporting the SIFI effect was plausibly an artifact from not considering the height dependences of $\overline{r_{ie}}$ in the TIC-2B tops and $\alpha_{2/1}$, which both decrease as altitude increases in the lower troposphere.

5. Discussion

5.1. Index Validation

[34] The index α is meant to be used only as an indicator of sulphate concentrations in the Arctic atmosphere. It is designed following theoretical considerations of how an Arctic haze mixture (not exclusively sulphates) is most likely to affect the lidar backscattering fields, and it is sensitive to unmasked clouds, sea salt and possibly other aerosol mixtures like the mineral dust particles that sulphate droplets are believed to coat and deactivate as IFN. These limitations must be kept in mind. On the other hand, in the absence of a pan-Arctic in situ sulphate concentration data set or of a better satellite-derived product, such an index is an appropriate sulphate concentration proxy and may be useful for locating Arctic haze, away from open waters.

[35] As can be seen in Figure 5, the $\alpha_{2/1}$ signal averaged within a 500 km wide box centered on the Zeppelin location may capture variations of measured sulphate concentrations, particularly when sodium concentrations remain low. However, it is clear that some high values in $\alpha_{2/1}$ are better explained by a sodium storm, and determination coefficients (R^2) between the various index series (differing by their w_β/w_χ ratio) and the (total or non-sea-salt) sulphate concentrations remain relatively low. These low values are due to both partial inadequacy of the indicator and inescapable limitations in the validation methodology adopted. Inadequacy of the sulphate concentration proxy is expected through potential sensitivity to other parameters. The marine aerosol is difficult to separate from Arctic haze on the basis of the color ratio, and we must also rely on previous knowledge of the geographical and vertical extensions of these two different mixtures when interpreting $\alpha_{2/1}$ distributions in Figure 6. Methodological limitations include the spatial mismatch between satellite trajectories and the station, the fact that overpasses are temporally concentrated within a few hours whereas the in situ instrument averages aerosol data over the whole day, and the exclusion of below-cloud aerosols from the satellite data, reducing statistics and possibly introducing a bias. Some pollution events may pass through the station one day and be crossed by the satellite trajectories the day after (or never), and vice versa. To strengthen the analysis, in situ sulphate and sodium particle number size distributions could be implemented, since the index may correlate better with the fine mode rather than the bulk mass. Such size distributions (e.g., from the EMEP project CREATE) were not available for winter-07 and winter-08 at the moment of the analysis. The weakening of the correlations when we replace $[SO_4]^{all}_{tot}$ with $[SO_4]^{all}_{nss}$ may result from underestimation of the sea salt fine-mode fraction.

[36] We can also evaluate our thinking that $\alpha_{2/1}$ is indicative of the sulphate concentration by examining the patterns obtained in Figure 6 in light of information in the literature about the sulphate field. For example, the patterns we observe in the present study are in general agreement with numerical simulation results obtained by *Christensen* [1997]. His results suggest that sulphur transits through the High Arctic (northward of 74.5°N) mostly within the Eastern Russia–Beaufort Sea–Canadian Archipelago (EBC) sectors during winter (1991–1994), with the most important positive flux within 45–135°E and the most important negative flux within 75–165°W, for the lowest 3 km asl. However, the analyzed $\alpha_{2/1}$ and modeled $[SO_4]_{tot}$ patterns do not match perfectly. Differences are partially due to (1) not considering the same layers, (2) the absence of in-cloud and below-cloud sulphate contributions in $\alpha_{2/1}$, (3) sulphate emissions having changed substantially since 1991–1994 [*Quinn et al.*, 2007], (4) the circulation variability strongly modulating sulphur injection fluxes from one year to the other [*Eckhardt et al.*, 2003], (5) limitations of the index, and (6) biases in the numerical simulation.

[37] As a proxy for sulphate concentrations, α could certainly be improved. To achieve this, more aircraft-assisted field campaigns are needed to determine the bulk depolarization and color ratio for clouds and aerosol mixtures. For example, *Liu et al.* [2002] have computed that only a small proportion of clouds should exhibit a color ratio smaller than 0.54. However, we found that after ONA increase these proportions were 24% for (TIC-2A + TIC-2B + TIC-2D) and 60% for TIC-1 throughout the Arctic (18 and 52% for winter-07). It would therefore seem that the separation criterion is not as sharp as what the calculations of *Liu et al.* [2002] indicate. Many misclassified TIC-1 bins can thus score high in g (χ) (although it is not fully understood why the overlap gets greater after ONA change). When plotting the χ distribution for all bins (not shown), we obtain two modes which separate at $\chi \approx 0.55$, therefore confirming the splitting criterion for ice clouds and aerosol layers obtained by *Liu et al.* [2002]. However, the degree of overlap that we found between aerosol and cloud

χ distributions is greater, since in the real atmosphere haze and ice crystals are mixed within the same volumes. The depolarization ratio, which is not used in the current version of the index (but previously used in the AWAC4 algorithm for segregating TIC-1 from non-cloudy bins), could be incorporated. However, as for the color ratio, a caveat is that the presence of ice crystals within haze-dominated volumes would bias the depolarization ratio [*Bourdages et al.*, 2009]. The relative humidity, which strongly influences the size of hygroscopic particles and consequently their contribution to β_{532} and χ [*Sasano and Browell*, 1989], could also be used. A-Train water vapor products (e.g., AIRS) have unfortunately too low vertical and horizontal resolutions to be meaningfully incorporated in our algorithm, unless we further smooth CloudSat and CALIPSO signals, in which case we would miss many TIC-1 tops and hardly be able to separate TIC-2A from TIC-2B.

[38] Prior to the validation/calibration of α, the feature classification algorithm may give results inconsistent with the reality owing to (1) uncertainties in the lidar fields used, (2) assumptions in the radar ice water content retrieval, (3) attenuation of the lidar beam, (4) spatial and temporal mismatch in satellites orbits, (5) averaging processes, and (6) feature classification algorithm assumptions and thresholds. GBM have discussed these sources of uncertainty in detail. Two modifications which could possibly improve the algorithm are (1) a treatment of the Rayleigh scattering, for assessing the molecular contribution to the backscattering (see *Haladay and Stephens* [2009] for methodology), and (2) a retrieval through the lidar equation, for having intrinsic (volume) instead of attenuated backscattering fields [see *Sasano and Browell*, 1989]. However, practical limitations could prevent these operations from leading to a significantly better classification in the end, because we would thus have to incorporate meteorological fields with a possibly high degree of uncertainty at the CloudSat resolution (like pressure and temperature for Rayleigh scattering) or make many assumptions to account for nonexistent information (like the lidar extinction-to-backscatter ratio for the retrieval). The lidar ratio depends on the microphysical, chemical and morphological properties of the ensemble of particles in the probed volume. *Ansmann and Müller* [2005] report typical values of 20–35 for marine aerosol and 35–70 for urban-like particles (akin to Arctic haze). For a sky devoid of radar-seen water content, the decrease in the signal attributed to haze and TIC-1 which would result from removing the molecular contribution (C_{Ray}) and the increase that would occur following a retrieval procedure (C_{att}) should both grow in magnitude for decreasing altitudes, and partially cancel each other. Correcting for the Rayleigh scattering without correcting for the attenuation would exacerbate the situation if $|C_{Ray}| < 2|C_{att}|$. Moreover, the retrieval within or below radar-seen clouds would often be performed on a depleted lidar signal, hence consisting of amplifying noise and leading to a divergent solution. Nevertheless, the effect (on α and F_{2B}) of performing these two operations needs to be investigated.

5.2. Implications for the SIFI Effect

[39] The AWAC4 algorithm allows for a spatial characterization of the features implied by the SIFI effect, namely ice clouds and aerosols. However, we face limitations when trying to interpret their spatial distributions in terms of the SIFI effect, and many assumptions are necessary. If we assume that $\alpha_{2/1}$ is a reasonable proxy for sulphate concentrations in the EBC sectors, there are two approaches we can explore for possibly validating or rejecting the SIFI plausible consequence according to which high sulphate concentrations favor cloud populations made of bigger ice crystals. The first consists of analyzing together the spatial distributions of $\alpha_{2/1}$ and F_{2B} (distributions test), and the second consists of correlating r_{ie} at the top of the TIC-2B with $\alpha_{2/1}$ just above (cloud top correlation test). For each test, we have developed an interpretation in terms of the SIFI effect, which we present here. Unless otherwise stated, we discuss the period after ONA increase.

[40] By comparing the $\alpha_{2/1}$ and F_{2B} patterns, we may establish our first conclusion that there is no evidence of a strong local impact of the SIFI effect in EBC sectors. Indeed in this case, we could reasonably expect $\alpha_{2/1}$ maxima (e.g., over Laptev Sea and Norilsk area, in the south of the Taimyr Peninsula) to correspond to F_{2B} maxima in some altitude layer, and it is generally not the case. If the SIFI is effective around Norilsk, it could mean (1) that other variables like supersaturation production rate and IFN availability influence F_{2B} more strongly, (2) that cloud-free sulphate concentration patterns are not representative of the total sulphate concentration patterns, (3) that the increase in CCN caused by sulphates masks the SIFI effect, and/or (4) that winds combined to the TIC-2 development time scale cause patterns not to overlap. We have inspected the average vector field of winds at 700 mb over winter-08 and winter-09 (not shown), obtained from the NCEP/NCAR reanalysis [*Kalnay et al.*, 1996]. It appears that prevalent winds were mostly zonal along the Eurasian northern coast, had a higher northward component over the Laptev and Chukchi Seas, and exited the Arctic Ocean mostly over the western part of the Canadian Archipelago. Wind patterns at 1000 mb, 925 mb and 850 mb in the EBC sectors could roughly be described the same way. The high F_{2B} values found over the Beaufort Sea and the eastern part of the Eastern Russia sectors are then located downwind of the high $\alpha_{2/1}$ values found over Eastern Russia, in terms of the prevalent circulation during the period. At this stage, it would be premature to claim that this picture provides firm support for the SIFI effect. A numerical model simulating the development of TIC-1/2A and TIC-2B systems on the aerosol field would be needed to conclude whether the SIFI effect is required to explain the $\alpha_{2/1}$ and F_{2B} spatial distributions. A second conclusion that may be drawn is that sulphates are not locally required in order to have a high TIC-2B fraction in the lower troposphere. Indeed, we find high F_{2B} values over North Atlantic, whereas high $\alpha_{2/1}$ values in the lowest layer are often due to the marine aerosol, with plausibly a small contribution from sea salt sulphates (the $\alpha_{2/1}$ pattern in the 1500–3000 m layer suggests that anthropogenic sulphates may relatively often reach the northern part of that sector, but that its southern part remains less polluted). Plausible explanations for North Atlantic high F_{2B} values are an important IFN deficiency in the marine aerosol [*Pruppacher and Klett*, 1997] and a sea salt–induced freezing inhibition effect.

[41] GBM found a small but statistically significant correlation ($r_{pea} \cong 0.10$) between the ice effective radius in

TIC-2B tops and above-cloud α (using a different version of the index, but with a similar meaning) and argued it would have been higher had it been possible to use a proxy for in-cloud sulphate concentrations. That finding suggested that sulphates favor cloud populations made of larger ice crystals. However, the results we obtained in this study, by analyzing the same correlation at a deeper level, show no evidence of a correspondence between above-cloud sulphate concentrations and cloud top r_{ie} in the EBC sectors. Moreover, they suggest that previous results were an artifact emerging from not considering the height dependence of $\overline{r_{ie}}$ and $\overline{\alpha_{2/1}}$. Without an indication that the above-TIC-2B sulphate concentrations are correlated with the in-TIC-2B concentrations, present results may not be clearly interpreted as evidence that high sulphate concentrations do not perceptibly favor cloud populations made of bigger ice crystals. In view of the limitations of interpreting the $\alpha_{2/1}$ signal in terms of sulphate concentrations when ice crystals are absent, it is unthinkable to retrieve any information about the in-cloud sulphate concentrations with the AWAC4 algorithm alone, and airborne measurements are needed for firmer conclusions. Concerning the uncertainty associated with the CloudSat r_{ie} product (about 20% in average), we conceive no indication of a bias which could have caused the null correlation (and/or the positive correlation when we do not segregate data by height intervals). A first reason we could invoke to explain an eventual weak SIFI effect is an overestimation of the importance of the deposition mode for Arctic winter ice nucleation. The relative importance of the nucleation modes is temperature and RH_i dependent [*Pruppacher and Klett*, 1997], and the SIFI effect strength has likely the same dependences. Also, if the SIFI effect is important in one of the nucleation modes active at liquid saturation, it may conceivably be masked by the action of sulphates in the condensation process. Indeed, sulphate particles contribute to increase the CCN concentration in Arctic haze, potentially counterbalancing the SIFI effect on the ice crystal number density.

[42] An alteration of the cloud microphysical properties may have considerable climate effects. In the High Arctic, if a transfer from TIC-2A to TIC-2B occurrence is caused by the SIFI effect, it may possibly lead to the dehydration-greenhouse feedback (DGF) [*Girard et al.*, 2005]. However, this mechanism has originally been schematized for understanding the radiative effects of (clear-sky) dehydrating diamond dust within the boundary layer [*Blanchet and Girard*, 1994]. Because the SIFI effect is the DGF trigger, results from the present paper render unclear if the mechanism may be transposed to the free troposphere. If further research suggests it is the case, the DGF mechanism should be conceptually reformulated, notably concerning the cooling propagation, and its conditions of applicability should be specified. Even concerning the boundary layer, it has been argued by *Lesins et al.* [2009] that a DGF-like mechanism can hardly act in topographic sectors like the Canadian Archipelago. In such areas, clear-sky precipitating ice crystal events may occur after snow has been blown off from surrounding higher terrain tens of kilometers away, since these ice crystals may then moisten the layers they cross rather than dehydrating them (this objection does not apply over the ice-covered Arctic Ocean). Overall, it remains plausible that the SIFI effect triggers a DGF-like chain of causation involving a cooling anomaly throughout the Arctic. The strength of this perturbation must be assessed (even if this is difficult, considering that the mechanism cannot be disentangled from the myriad of other feedbacks in the Arctic climate system), because strong variations in the anthropogenic sulphate injections since the beginning of the industrial era may have implied strong surface temperature changes. If the DGF mechanism is strong, it could have caused a pan-Arctic cooling trend (the accentuation of a cooling anomaly) during most of the 20th century, as well as a warming trend since about 1990, after the European acid rain fight and Soviet industrial collapse have caused a decreasing trend in sulphate concentrations, as observed at eight monitoring Arctic stations [*Quinn et al.*, 2007].

6. Conclusion

[43] The sulphate-induced freezing inhibition (SIFI) effect, an hypothesis according to which sulphates contribute to inhibit the onset of ice crystal formation by deactivating ice-forming nuclei, has a potential consequence that may be investigated using the CloudSat and CALIPSO data sets, that is, the idea that higher sulphate concentrations favor ice clouds made of larger ice crystals. Theoretical considerations have been used for designing a simple index (α) based on the backscattering at 532 nm (β_{532}) and the color ratio (χ) from the CALIPSO lidar measurements. After comparing winter-07 and winter-08 Zeppelin station sulphate concentrations with α averaged within a 500 km wide and 500 m thick box centered on the station, we believe that such an index is an appropriate proxy for the sulphate concentrations in non-cloudy probed volumes of the Arctic atmosphere, and useful for the study of the SIFI effect. Limitations include α sensitivity to misclassified clouds and other aerosol compounds, notably sea salt. We tested the SIFI hypothesis in two ways. From the distributions test, we found no evidence of a strong local SIFI effect, but argued that having higher TIC-2B (clouds supposedly favored by the SIFI effect) fraction values downwind higher α values is consistent with a SIFI effect acting on a relatively long time scale. From the cloud top correlation test, we found practically no correlation between the ice effective radius at the top of TIC-2B and the sulphate index just above, suggesting a weak SIFI effect. However, an inescapable limitation inherent to the methodology of this test, that is, the fact that we use an above-cloud instead of an in-cloud sulphate concentration proxy, renders the SIFI effect validation/refutation an unclosed subject. Airborne measurements of the ice effective radius and aerosol properties within ice clouds are definitively needed to obtain firmer conclusions.

[44] **Acknowledgments.** P.G. acknowledges the Ouranos Consortium and the National Sciences and Engineering Research Council of Canada (NSERC) for financial support. The funding for this research was also supported by the NSERC through its International Polar Year 2007–2008 program. We also acknowledge the NASA Langley Research Center/Atmospheric Science Data Center, from which CALIPSO data were obtained, and the NASA CloudSat project. The Norwegian Pollution Control Agency (SFT) finances the monitoring program at Zeppelin, and the

Norwegian Institute for Air Research (NILU) is acknowledged for additional support.

References

Aas, W., S. Solberg, S. Manø, and K. E. Yttri (2008), Monitoring of long-range transported air pollutants, 2007 (in Norwegian), *OR 29/2008, SFT Rapp. 1033/2008*, Norw. Inst. for Air Res., Kjeller, Norway.

Andreae, M. O., D. A. Hegg, and U. Baltensperger (2008), Sources and nature of atmospheric aerosols, in *Aerosol Pollution Impact on Precipitation: A Scientific Review*, edited by Z. Levin and W. R. Cotton, chap. 3, pp. 45–90.

Ansmann, A., and D. Müller (2005), Lidar and atmospheric aerosol particles, in *Lidar: Range-Resolved Optical Remote Sensing of the Atmosphere*, edited by C. Weitkamp, chap. 4, pp. 105–141.

Arctic Monitoring and Assessment Programme (1998), AMAP assessment report: Arctic pollution issues, 859 pp., Oslo.

Austin, R. T., A. J. Heymsfield, and G. L. Stephens (2009), Retrieval of ice cloud microphysical parameters using the CloudSat millimeter-wave radar and temperature, *J. Geophys. Res.*, *114*, D00A23, doi:10.1029/2008JD010049.

Bertram, A. K., D. D. Patterson, and J. J. Sloan (1996), Mechanisms and temperatures for the freezing of sulfuric acid aerosols measured by FTIR extinction spectroscopy, *J. Phys. Chem.*, *100*(6), 2376–2383, doi:10.1021/jp952551v.

Bigg, E. K. (1980), Comparison of aerosol at four baseline atmospheric monitoring stations, *J. Appl. Meteorol.*, *19*, 521–533, doi:10.1175/1520-0450(1980)019<0521:COAAFB>2.0.CO;2.

Blanchet, J.-P., and E. Girard (1994), Arctic greenhouse effect, *Nature*, *371*, 383, doi:10.1038/371383a0.

Blanchet, J.-P., and R. List (1983), Estimation of optical properties of Arctic haze using a numerical model, *Atmos. Ocean*, *21*(4), 444–465.

Borys, R. D. (1989), Studies of ice nucleation by Arctic aerosols on AGASP-II, *J. Atmos. Chem.*, *9*, 169–185, doi:10.1007/BF00052831.

Bourdages, L., T. J. Duck, G. Lesins, J. R. Drummond, and E. W. Eloranta (2009), Physical properties of High Arctic tropospheric particles during winter, *Atmos. Chem. Phys. Discuss.*, *9*, 7781–7823, doi:10.5194/acpd-9-7781-2009.

Broeckner, W. S., and T.-H. Peng (1982), *Tracers in the Sea*, pp. 26–27, Eldigio, Palisades, N. Y.

Carlson, T. N. (1981), Speculations on the movement of polluted air to the Arctic, *Atmos. Environ.*, *15*, 1473–1477, doi:10.1016/0004-6981(81)90354-1.

Christensen, J. H. (1997), The Danish Eulerian hemispheric model: A three-dimensional air pollution model used for the Arctic, *Atmos. Environ.*, *31*, 4169–4191, doi:10.1016/S1352-2310(97)00264-1.

Clarke, A. (1989), In-situ measurements of the aerosol size distributions, physicochemistry and light absorption properties of Arctic haze, *J. Atmos. Chem.*, *9*, 255–266, doi:10.1007/BF00052836.

Eastwood, M. L., S. Cremel, M. Wheeler, B. J. Murray, E. Girard, and A. K. Bertram (2009), Effects of sulfuric acid and ammonium sulfate coatings on the ice nucleation properties of kaolinite particles, *Geophys. Res. Lett.*, *36*, L02811, doi:10.1029/2008GL035997.

Eckhardt, S., A. Stohl, S. Beirle, N. Spichtinger, P. James, C. Forster, C. Junker, T. Wagner, U. Platt, and S. G. Jennings (2003), The North Atlantic Oscillation controls air pollution transport to the Arctic, *Atmos. Chem. Phys. Discuss.*, *3*, 3222–3240, doi:10.5194/acpd-3-3222-2003.

Garrett, T. J., and L. L. Verzella (2008), Looking back: An evolving history of Arctic aerosols, *Bull. Am. Meteorol. Soc.*, *89*, 299–302, doi:10.1175/BAMS-89-3-299.

Girard, E., and A. Stefanof (2007), Assessment of the dehydration-greenhouse feedback over the Arctic during February 1990, *Int. J. Climatol.*, *27*, 1047–1058, doi:10.1002/joc.1455.

Girard, E., J.-P. Blanchet, and Y. Dubois (2005), Effects of arctic sulphuric acid aerosols on wintertime low-level atmospheric ice crystals, humidity and temperature at Alert, Nunavut, *Atmos. Res.*, *73*, 131–148, doi:10.1016/j.atmosres.2004.08.002.

Gong, S. L., and L. A. Barrie (2003), Simulating the impact of sea salt on global nss sulphate aerosols, *J. Geophys. Res.*, *108*(D16), 4516, doi:10.1029/2002JD003181.

Grenier, P., J.-P. Blanchet, and R. Munoz-Alpizar (2009), Study of polar thin ice clouds and aerosols seen by CloudSat and CALIPSO during mid-winter 2007, *J. Geophys. Res.*, *114*, D09201, doi:10.1029/2008JD010927.

Haladay, T., and G. Stephens (2009), Characteristics of tropical thin cirrus clouds deduced from joint CloudSat and CALIPSO observations, *J. Geophys. Res.*, *114*, D00A25, doi:10.1029/2008JD010675.

Hara, K., S. Yamagata, T. Yamanouchi, K. Sato, A. Herber, Y. Iwasaka, M. Nagatani, and H. Nakata (2003), Mixing states of individual aerosol particles in spring Arctic troposphere during ASTAR 2000 campaign, *J. Geophys. Res.*, *108*(D7), 4209, doi:10.1029/2002JD002513.

Hunt, W. H., D. M. Winker, M. A. Vaughan, K. A. Powell, P. L. Lucker, and C. Weimer (2009), CALIPSO lidar description and performance assessment, *J. Atmos. Oceanic Technol.*, *26*, 1214–1228, doi:10.1175/2009JTECHA1223.1.

Kahn, B. H., et al. (2007), Cloud type comparisons of AIRS, CloudSat, and CALIPSO cloud height and amount, *Atmos. Chem. Phys. Discuss.*, *7*, 13,915–13,958, doi:10.5194/acpd-7-13915-2007.

Kalnay, E., et al. (1996), The NCEP/NCAR Reanalysis 40-year Project, *Bull. Am. Meteorol. Soc. 77*, 437–471, doi:10.1175/1520-0477(1996)077<0437:TNYRP>2.0.CO;2.

Law, K. S., and A. Stohl (2007), Arctic air pollution: Origins and impacts, *Science*, *315*, 1537–1540, doi:10.1126/science.1137695.

Lesins, G., L. Bourdages, T. J. Duck, J. R. Drummond, E. W. Eloranta, and V. P. Walden (2009), Large surface radiative forcing from topographic blowing snow residuals measured in the High Arctic at Eureka, *Atmos. Chem. Phys.*, *9*, 1847–1862, doi:10.5194/acp-9-1847-2009.

Liu, Z., M. Vaughan, L. Poole, C. Hostetler, and D. Winker (2002), Scene classification for the CALIPSO lidar, paper presented at ILRC 2002, Quebec City, Que., Canada.

Lohmann, U., and E. Roeckner (1996), Design and performance of a new cloud microphysics scheme developed for the ECHAM general circulation model, *Clim. Dyn.*, *12*, 557–572, doi:10.1007/BF00207939.

Lowenthal, D. H., R. D. Borys, T. W. Choularton, K. N. Bower, M. J. Flynn, and M. W. Gallagher (2004), Parameterization of the cloud droplet-sulfate relationship, *Atmos. Environ.*, *38*, 287–292, doi:10.1016/j.atmosenv.2003.09.046.

Marcolli, C., S. Gedamke, T. Peter, and B. Zobrist (2007), Efficiency of immersion mode ice nucleation on surrogates of mineral dust, *Atmos. Chem. Phys.*, *7*, 5081–5091, doi:10.5194/acp-7-5081-2007.

Norwegian Institute for Air Research (1996), EMEP manual for sampling and chemical analysis, *EMEP/CCC-Report 1/95*, Kjeller, Norway.

Omar, A. H., and T. Babakaeva (2004), Aerosol optical properties derived from lidar observations using cluster analysis, in *Geoscience and Remote Sensing Symposium, 2004: IGARSS'04*, vol. 3, pp. 2212–2215, Inst. of Electr. and Electron. Eng., Piscataway, N. J.

Onasch, T. B., R. L. Siefert, S. D. Brooks, A. J. Prenni, B. Murray, M. A. Wilson, and M. A. Tolbert (1999), Infrared spectroscopic study of the deliquescence and efflorescence of ammonium sulfate aerosol as a function of temperature, *J. Geophys. Res.*, *104*(D17), 21,317–21,326, doi:10.1029/1999JD900384.

Pruppacher, H. R., and J. D. Klett (1997), *Microphysics of Clouds and Precipitation*, 2nd ed., 954 pp., Kluwer Acad., Boston, Mass.

Quinn, P. K., G. Shaw, E. Andrews, E. G. Dutton, T. Ruoho-Airola, and S. L. Gong (2007), Arctic haze: Current trends and knowledge gaps, *Tellus, Ser. B*, *59*, 99–114.

Rahn, K. A. (1981), Relative importances of North America and Eurasia as sources of Arctic aerosol, *Atmos. Environ.*, *15*, 1447–1455, doi:10.1016/0004-6981(81)90351-6.

Sasano, Y., and E. V. Browell (1989), Light scattering characteristics of various aerosol types derived from multiple wavelength lidar observations, *Appl. Opt.*, *28*(9), 1670–1679, doi:10.1364/AO.28.001670.

Sassen, K. (1991), The polarization lidar technique for cloud research: A review and current assessment, *Bull. Am. Meteorol. Soc.*, *72*, 1848–1866, doi:10.1175/1520-0477(1991)072<1848:TPLTFC>2.0.CO;2.

Schutgens, N., and D. P. Donovan (2004), Retrieval of atmospheric reflectivity profiles in case of long radar pulses, *Atmos. Res.*, *72*, 187–196, doi:10.1016/j.atmosres.2004.03.014.

Shaw, G. E., K. Stamnes, and Y. X. Hu (1993), Arctic haze: Perturbation to the radiation field, *Meteorol. Atmos. Phys.*, *51*, 227–235, doi:10.1007/BF01030496.

Sirois, A., and L. A. Barrie (1999), Arctic lower tropospheric aerosol trends and composition at Alert, Canada: 1980–1995, *J. Geophys. Res.*, *104*(D9), 11,599–11,618, doi:10.1029/1999JD900077.

Stephens, G. L., et al. (2002), The CloudSat mission and the A-Train: A new dimension of space-based observations of clouds and precipitation, *Bull. Am. Meteorol. Soc.*, *83*, 1771–1790, doi:10.1175/BAMS-83-12-1771.

Tang, I. N., and H. R. Munkelwitz (1994), Water activities, densities, and refractive indices of aqueous sulfates and sodium nitrate droplets of atmospheric importance, *J. Geophys. Res.*, *99*(D9), 18,801–18,808, doi:10.1029/94JD01345.

Waggoner, A. P., and R. E. Weiss (1980), Comparison of fine particle mass concentration and light scattering extinction in ambient aerosol, *Atmos. Environ.*, *14*, 623–626, doi:10.1016/0004-6981(80)90098-0.

Wandinger, U. (2005), Introduction to lidar, in *Lidar: Range-Resolved Optical Remote Sensing of the Atmosphere*, edited by C. Weitkamp, chap. 1, pp. 1–18, Springer, New York.

Welti, A., F. Lüönd, O. Stetzer, and U. Lohmann (2009), Influence of particle size on the ice nucleating ability of mineral dusts, *Atmos. Chem. Phys. Discuss.*, *9*, 6929–6955, doi:10.5194/acpd-9-6929-2009.

Yamanouchi, T., et al. (2005), Arctic Study of Tropospheric Aerosol and Radiation (ASTAR) 2000: Arctic haze case study, *Tellus, Ser. B*, *57*, 141–152.

Yu, H., M. Chin, L. A. Remer, R. G. Kleidman, N. Bellouin, H. Bian, and T. Diehl (2009), Variability of marine aerosol fine-mode fraction and estimates of anthropogenic aerosol component over cloud-free oceans from the Moderate Resolution Imaging Spectroradiometer (MODIS), *J. Geophys. Res.*, *114*, D10206, doi:10.1029/2008JD010648.

J.-P. Blanchet and P. Grenier, Institut des Sciences de l'Environnement, Université du Québec à Montréal, P.O. Box 8888, Station Downtown, Montreal, QC H3C 3P8, Canada. (grenier@sca.uqam.ca)